Available online at www.sciencedirect.com
ScienceDirect
Catalysis Today 131 (2008) 42–54
CATALYSIS TODAY
www.elsevier.com/locate/cattod

A comparative investigation on the properties of Cr-SBA-15 and CrO_x/SBA-15

Lei Zhang [a], Yanhui Zhao [a], Hongxing Dai [a,*], Hong He [a], C.T. Au [b,**]

[a] *Laboratory of Catalysis Chemistry and Nanoscience, Department of Chemistry and Chemical Engineering, College of Environmental and Energy Engineering, Beijing University of Technology, Beijing 100022, China*
[b] *Department of Chemistry, Center for Surface Analysis and Research, Hong Kong Baptist University, Kowloon Tong, Hong Kong, China*

Available online 26 November 2007

Abstract

High-surface area and well-ordered mesoporous Cr-incorporated SBA-15 (Cr-SBA-15) and SBA-15-supported chromia (CrO_x/SBA-15) with Cr surface density = 0.05–1.11 Cr-atom/nm^2 have been prepared, respectively, using the one-step synthesis and incipient wetness impregnation method, and characterized by AAS, XRD, BET, ESEM, TEM, XPS, laser Raman, UV-Vis, FT-IR, and H_2-TPR. It is observed that the Cr-SBA-15 and CrO_x/SBA-15 samples showed an evolution of surface morphology from long chain-shaped to short rod-like and further to an irregularly spherical architecture at elevated Cr content, which might arise from the interaction of Cr ions or CrO_x domains with SBA-15. There were co-presence of tetrahedrally coordinated mono- and poly-chromate (Cr^{6+}) as well as octahedrally coordinated Cr^{3+} species in Cr-SBA-15 and CrO_x/SBA-15, with the Cr^{6+} species being dominant at Cr surface density $\leq$0.22 Cr-atom/nm^2 in Cr-SBA-15 and Cr $\leq$0.54 Cr-atom/nm^2 in CrO_x/SBA-15, whereas the amount of the Cr^{3+} species increased markedly at Cr surface density $\geq$0.53 Cr-atom/nm^2 due to the formation of crystal Cr_2O_3 phase. Maximal Cr incorporation into Cr-SBA-15 and one monolayer surface CrO_x coverage on CrO_x/SBA-15 occurred at Cr surface density $\leq$0.53 Cr-atom/nm^2 and $<$1.11 Cr-atom/nm^2, respectively. The CrO_x/SBA-15 samples exhibited better reducibility than the Cr-SBA-15 samples, with the best reducibility exhibited at Cr surface densities of 0.54 and 0.12 Cr-atom/nm^2, respectively.

Keywords: Mesoporous silica SBA-15; Chromium-incorporated SBA-15; SBA-15-supported chromia; Surface chromia species; Reducibility; Surface morphology

1. Introduction

Although transition metal oxides (MO_x) are a kind of effective catalytic materials for many reactions, their catalytic performance is limited by the low-surface areas. Incorporating the M^{n+} ions to a framework of high-surface area mesoporous molecular sieves (MMS) or loading their oxides onto the surfaces of these porous materials is a good strategy to circumvent the above limitation. The incorporation of M^{n+} to or loading of MO_x on porous materials can result in high dispersion of M^{n+} or MO_x domains. In the selective oxidation of light alkanes, vanadia-, molybdena-, and chromia-based materials exhibit high catalytic activities, especially the chromium-containing ones [1,2]. Silica- and alumina-supported chromia were industrially used for the production of polyethylene and light alkenes (e.g. propylene and isobutene) through the dehydrogenation of the corresponding alkane counterparts [3,4]. Supported vanadia and chromia show good photocatalytic activities in the degradation or selective oxidation of organic compounds under ultraviolet or even visible light irradiation [5,6]. Mesoporous materials such as M41S (e.g. MCM-41, MCM-48 or MCM-50) and SBA-15 possess high-surface areas, uniform pore size distributions, and large pore sizes. The unique characteristics of these materials render them appropriate support materials for catalytic reactions.

In recent years, the synthesis, characterization, and application of metal-incorporated mesoporous materials in catalysis, separation, and adsorption investigations have incited great interest [7–11]. Compared to M41S, SBA-15 (synthesized with triblock copolymer as surfactant under strongly acidic conditions) exhibits larger pore size and thicker pore wall. The improved hydrothermal stability makes the latter promising catalytic materials [12,13]. Usually, ''direct-synthesis (i.e. one-step synthesis)'' [14–19] and ''incipient wetness impregnation''

* Corresponding author. Tel.: +86 10 6739 6588; fax: +86 10 6739 1983.
** Co-corresponding author.
E-mail addresses: hxdai@bjut.edu.cn (H. Dai), pctau@hkbu.edu.hk (C.T. Au).

0920-5861/$ – see front matter © 2007 Elsevier B.V. All rights reserved.
doi:10.1016/j.cattod.2007.10.017

[20–24] methods are used for the introduction of M^{n+} ions into the lattices of porous materials and for the generation of loaded MO_x, respectively. In order to introduce functionality and to broaden applications, various metal ions such as Al [18,19], Ti [15–17,25,26], and Fe [14] have been successfully incorporated into the framework of SBA-15. By adjusting the pH value to 1.5, Yue et al. synthesized Al-SBA-15 [18]; by controlling the hydrolysis process of the Si precursor in a fluoride media, Zhang et al. fabricated Ti-SBA-15 [25]. With the assistance of microwave irradiation, Newalkar et al. generated Ti-SBA-15 via hydrothermal treatment of Ti and Si precursors [26]. There are reports relevant to the synthesis of Cr-incorporated mesoporous materials [9,11,27–30]. For example, the employment of the hydrothermal synthesis and template-ion exchange method could generate a Cr-MCM-41 that showed high catalytic performance for the oxidation of methane and propane [9]; using templating/hydrothermal method, Zhu et al. [27] obtained a series of chromium-incorporated MCM-41 with various Si/Cr molar ratios. It is generally believed that via the ''direct-synthesis'' pathway, one can incorporate only a small amount of M^{n+} ions to the final mesoporous products. Using the incipient wetness impregnation or molecular designed dispersion (MDD) method, however, one can load a higher amount of the desired active component onto the surfaces of mesoporous materials [20–24]. For example, by adopting an alcoholic impregnation method, Liu et al. [20] prepared the VO_x/SBA-15 catalysts that showed high propene selectivity in the oxidative dehydrogenation of propane; by employing the MDD method and with metal acetylacetonate complexes as precursor, Segura et al. [23] fabricated SBA-15-supported TiO_x-VO_x mixed oxide catalysts in a controlled manner.

It has been known that the local coordination environments (i.e. existence modes) of M^{n+} ions located in the lattice and on the surface of MMS (denoted as M-MMS and MO_x/MMS, respectively, hereinafter) are different [30]. The difference in existence modes of the M^{n+} species results in discrepancy in physicochemical property of M-MMS and MO_x/MMS. The most common coordination modes are tetrahedral and octahedral [30–35]. That is to say, through the modification of MMS by incorporating M^{n+} ions into the porous MMS framework or by depositing MO_x onto the MMS surface, one can manipulate the physicochemical properties of the porous materials. Recently, we have synthesized several series of Cr- and V-incorporated MMS (such as SBA-15, MCM-48) and MMS-supported CrO_x and VO_x catalysts by means of surfactant-assisted hydrothermal and incipient wetness impregnation methods, respectively. In this paper, we report the synthesis strategies and physicochemical properties of Cr-incorporated SBA-15 and SBA-15-loaded CrO_x catalysts of different Cr contents.

2. Experimental

2.1. Catalyst preparation

The mesoporous silica SBA-15 was synthesized by adopting the procedure reported by Zhao et al. [12]. In a typical synthesis, 2.0 g of poly(ethylene glycol)-block-poly(propylene glycol)-block-poly(ethylene glycol) ($EO_{20}PO_{70}EO_{20}$, P123, averaged molecular weight = 5800, Aldrich) was dissolved in a mixture of 15 ml deionized water and 60 ml 2 M HCl (Beijing Chemical Reagents) under stirring. Then 4.25 g of tetraethyl orthosilicate (TEOS, 98%, Aldrich) was added dropwise to the solution at 40 °C. After being stirred continuously for 24 h, the mixture was transferred to a Teflon-lined stainless steel autoclave and placed in an oven at 100 °C for 48 h. The precipitate was in turn filtered, washed with deionized water and acetone, and dried at 100 °C for 3 h. The obtained powders were heated to 550 °C at a ramp rate of 1 °C/min and calcined at this temperature in air for 24 h.

Cr-incorporated SBA-15 with various $n_{Cr}/n_{(Cr+Si)}$ molar ratios were synthesized using the P123-templated hydrothermal method similar to that described elsewhere [14,36]. In a typical synthesis, 4.0 g of P123 was dispersed in 30 g of water. After stirring the mixture for 4 h, 70 ml of 0.29 M HCl were added and the solution was stirred for 2 h. Then 9.0 g of TEOS and an appropriate amount of chromium nitrate nonahydrate (>99.0%, Beijing Chemical Reagents) were added under stirring to the above homogeneous solution. After further stirring at 40 °C for 24 h, the resulted gel (molar composition $TEOS:Cr_2O_3:P123:HCl:H_2O \approx 1:0.0051–0.0376:0.016:0.47:129$) was transferred to an autoclave for hydrothermal processing at 100 °C for 48 h. The obtained mixtures were washed with deionized water, filtered, and dried at 120 °C overnight. With proper grinding, the obtained powders were heated in air from room temperature (RT) to 550 °C with a heating rate of 1 °C/min and kept at this temperature for 24 h. The received samples are denoted as xCr-SBA-15 (the nominal molar ratio $x = n_{Cr}/n_{(Cr+Si)} = 1.0–7.0$ mol%) hereinafter.

The CrO_x/SBA-15 samples of different chromium loadings $n_{Cr}/n_{(Cr+Si)}$ were prepared by adopting the incipient wetness impregnation approach. The SBA-15 was impregnated with an aqueous solution of a desired amount of chromium nitrate. The resulting material was then dried at 110 °C in air overnight and calcined in an O_2 flow of 30 ml/min from RT to 550 °C with a ramp of 1 °C/min and kept at this temperature for 2 h. The obtained samples are denoted as yCrO$_x$/SBA-15 (the nominal molar ratio $y = n_{Cr}/n_{(Cr+Si)} = 1.0–7.0$ mol%) hereinafter. For comparison, we also present the Cr surface density (Cr-atom/nm^2), i.e. the number of Cr atoms per unit surface area (in nm^2) of the xCr-SBA-15 or yCrO$_x$/SBA-15 sample (obtained based on results of AAS analysis) in Table 1.

2.2. Catalyst characterization

The atomic absorption spectroscopic (AAS) technique was used to determine the chromium content of each sample (HITACHI Z-8000). Before the AAS analysis, the samples were digested in a mixture of HF and HNO_3.

The crystal phase and pore structures of the samples were determined on an X-ray diffractometer (XRD, Bruker/AXS D8 Advance) operating at 40 kV and 200 mA using Cu Kα irradiation and nickel filter (λ = 0.15406 nm). The XRD

Table 1
Physical properties of *x*Cr-SBA-15 and *y*CrO_x/SBA-15 samples

*x*Cr-SBA-15 or *y*CrO_x/SBA-15[a]	Surface area (m^2/g)	n_{Si}/n_{Cr}[b]	Cr surface density (Cr-atom/nm^2)	Average pore size (nm)	Pore volume (cm^3/g)
SBA-15	796	–	–	5.6	0.98
1.0Cr-SBA-15	922	197.6 (99.0)	0.05	5.3	1.23
1.5Cr-SBA-15	790	131.7 (65.7)	0.09	5.1	1.00
2.0Cr-SBA-15	867	97.8 (49.0)	0.12	5.3	1.15
2.5Cr-SBA-15	850	81.3 (39.0)	0.14	5.0	1.05
4.0Cr-SBA-15	860	50.0 (24.0)	0.22	5.5	1.18
5.5Cr-SBA-15	947	18.6 (17.2)	0.53	5.0	1.18
7.0Cr-SBA-15	902	14.4 (13.3)	0.71	5.1	1.16
1.0CrO_x/SBA-15	573	115.1 (99.0)	0.15	5.6	0.80
1.5CrO_x/SBA-15	611	67.0 (65.7)	0.24	5.6	0.85
2.0CrO_x/SBA-15	600	52.5 (49.0)	0.31	5.5	0.83
4.0CrO_x/SBA-15	705	25.0 (24.0)	0.54	5.7	0.94
7.0CrO_x/SBA-15	601	13.7 (13.3)	1.11	5.3	0.78

[a] Nominal compositions: *x*, $y = n_{Cr}/n_{Si+Cr}$ mol%.
[b] Data were obtained from the results of AAS analysis and the data in parentheses were the nominal n_{Si}/n_{Cr} ratios.

patterns were recorded in the 2θ range of 0.6°–10° for small-angle profiles and 10°–80° for wide-angle profiles. Surface areas and pore size distributions as well as N_2 adsorption–desorption isotherms of the samples were measured via N_2 adsorption at −196 °C on a Micromeritics ASAP 2020 apparatus with all samples outgassed at 250 °C for 2 h under vacuum before measurement; surface areas and pore size distributions were calculated according to the BET and BJH (Barrett–Joyner–Halenda) method, respectively. The images of the samples were recorded by the use of an environmental scanning electron microscopy (ESEM, FEI Quanta 200) operating at 30 kV. Before being transferred into the ESEM chamber, a sample ultrasound-dispersed with ethanol was settled on a holder and then moved into the vacuum evaporator in which a thin gold film was deposited after sample drying. By means of a JEOL-2010 instrument (operating at 200 kV), transmission electron microscopy (TEM) images and selected area electron diffraction (SAED) patterns of samples were obtained.

X-ray photoelectron spectroscopy (XPS, VG CLAM 4 MCD analyzer) was employed to determine the O 1s, Cr 2p, and Si 2p binding energies of surface oxygen, chromium, and silicon species with Mg Kα ($h\nu$ = 1253.6 eV) as the excitation source. The instrumental resolution was 0.5 eV. Before XPS determination, the samples were calcined in O_2 (flow rate, 20 ml/min) at 600 °C for 1 h and then cooled to RT. After the above treatment, the samples were mounted and transferred to the spectrometer in a transparent GLOVE BAG (Instruments for Research and Industry, USA) filled with helium. The samples were then outgassed in the preparation chamber (10^{-5} Torr) for 0.5 h and introduced into the analysis chamber (3×10^{-9} Torr) for recording. The C 1s peak at 284.6 eV was taken as a reference for binding energy calibration.

Laser Raman spectra of the samples were obtained on a Raman spectrometer (Bruker RFS/100) equipped with a Nd:YAG laser (1064 nm) and an InGaAs detector; the laser power was 100 mW. The powdered samples were placed in a sample holder and recording (from 200 to 1200 cm^{-1} with a resolution of 4 cm^{-1}) was done in ambient atmosphere. With $BaSO_4$ being standard, UV–vis spectra of samples in the range of 200–800 nm were measured on a UV-Vis spectrophotometer (Shimadzu UV 2200). Fourier-transfer infrared spectroscopic (FT-IR) spectra (400–5000 cm^{-1} with a resolution of 0.4 cm^{-1}) of samples (1 wt% sample + 99 wt% KBr) were recorded on a Bruker Vertex 70 spectrometer.

Hydrogen temperature-programmed reduction (H_2-TPR) experiments were conducted with a sample (80–300 mg) first pretreated in situ in O_2 (flow rate = 40 ml/min) at 500 °C for 0.5 h in a quartz fixed-bed micro-reactor (i.d. = 6 mm). After cooling to RT in the same atmosphere, the sample was exposed to a flow (50 ml/min) of 5% H_2–95% He (v/v) and heated at a rate of 10 °C/min to 700 °C. The outlet gases were analyzed on-line over a MS equipment (HIDEN HPR20). The MS response was calibrated against that of the complete reduction of a known standard of powder CuO (Aldrich, 99.995%).

3. Results and discussion

3.1. Phase structures

Fig. 1 shows the small- and wide-angle XRD patterns of *x*Cr-SBA-15 and *y*CrO_x/SBA-15. It is observed from Fig. 1A and C that the XRD features of all the samples are rather similar, with three diffraction peaks at 2θ = 0.88°, 1.5°, and 1.8° that can be indexed as (1 0 0), (1 1 0), and (2 0 0) reflections, respectively. This kind of XRD profiles verifies the formation of typical hexagonally-structured SBA-15 silica with highly ordered mesoporous channels as reported by Zhao et al. [12]. The intensities of the diffraction peaks in the small-angle region of the *x*Cr-SBA-15 samples are similar except for the sample with Cr surface density = 0.12 Cr-atom/nm^2 which exhibits a higher intensity (Fig. 1A). The results indicated that the well-ordered pore structures of SBA-15 were basically retained in the *x*Cr-SBA-15 samples. On the contrary, with a rise in Cr surface density from 0.05 to 0.71 Cr-atom/nm^2, the *y*CrO_x/SBA-15 samples showed gradual decrease in intensity of diffraction

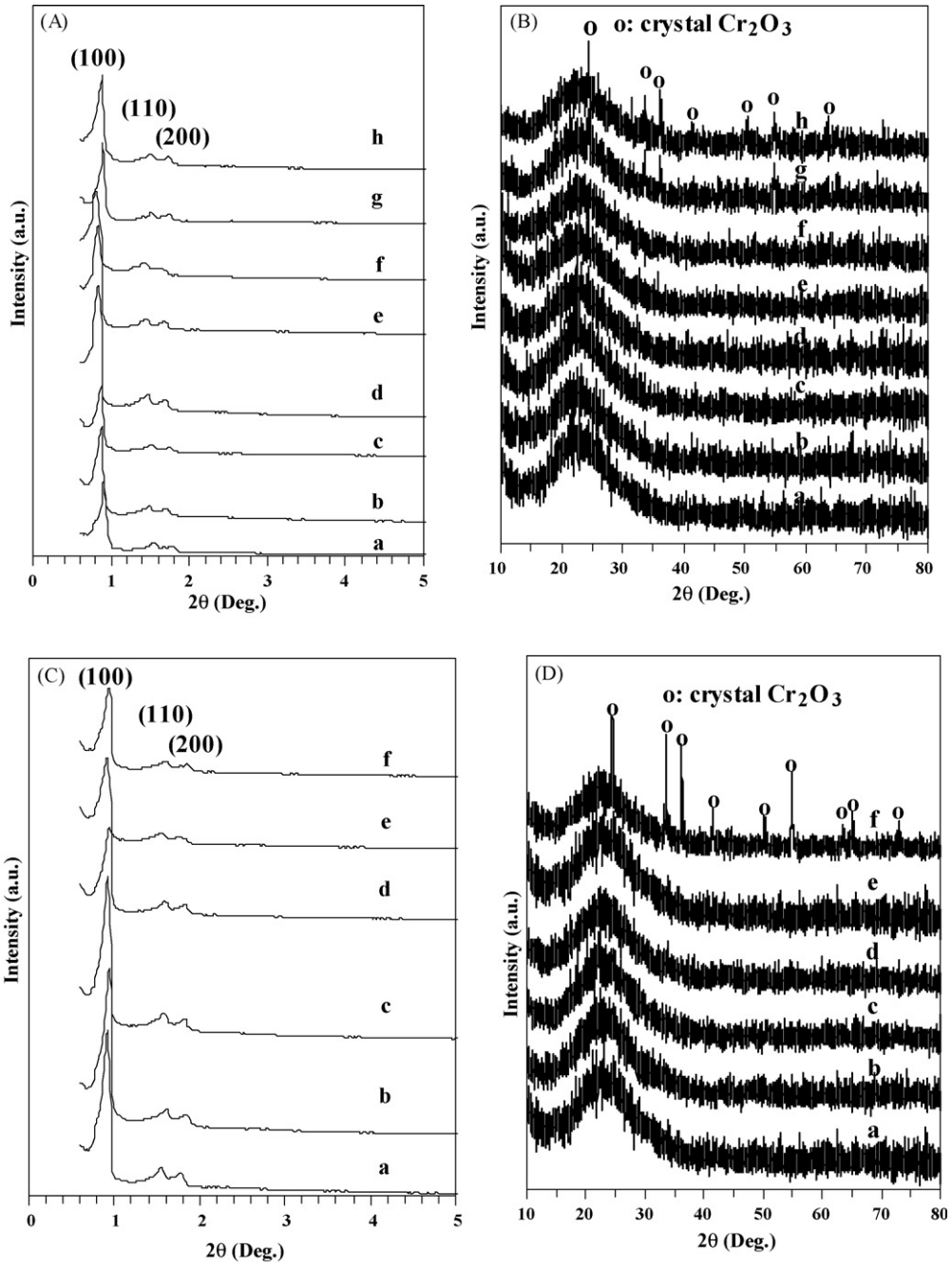

Fig. 1. Small- and wide-angle XRD patterns of (A and B) *x*Cr-SBA-15 with Cr surface density = 0 (a), 0.05 (b), 0.09 (c), 0.12 (d), 0.14 (e), 0.22 (f), 0.53 (g), and 0.71 (h) Cr-atom/nm^2, and (C and D) *y*CrO_x/SBA-15 with Cr surface density = 0 (a), 0.15 (b), 0.24 (c), 0.31 (d), 0.54 (e), and 1.11 (f) Cr-atom/nm^2.

peaks in the small-angle region (Fig. 1C), suggesting that there was a deterioration of the ordered pore structures. According to the wide-angle XRD patterns (Fig. 1B and D), diffraction signals at $2\theta = 24.5^\circ$, 33.6°, 36.2°, and 54.8° attributable to the hexagonal phase of Cr_2O_3 (JCPDS No.: 84-1616) were observed over the *x*Cr-SBA-15 and *y*CrO_x/SBA-15 samples with Cr surface density = 0.53 and 0.71 Cr-atom/nm^2 (Fig. 1B(g) and (h)) and 1.11 Cr-atom/nm^2 (Fig. 1D(f)), respectively. In other words, there was a small amount of crystalline Cr_2O_3 on Cr-SBA-15 with Cr surface density = 0.53 and 0.71 Cr-atom/nm^2 and on CrO_x/SBA-15 with Cr surface density = 1.11 Cr-atom/nm^2 whereas the majority of the chromium species of all the samples were amorphous. Due to the detection limitation of the XRD technique, the signals of Cr_2O_3 in the samples of lower Cr contents are hard to detect. In other words, it is hard to be conclusive if there were Cr incorporation to the skeleton of SBA-15 or not. Nonetheless, the Raman and XPS techniques are much more sensitive than the XRD technique in detecting the signals of Cr_2O_3, and the results so obtained are helpful to identify the position of Cr ions in Cr-SBA-15 as illustrated later in Section 3.4. Based on the above results, we purpose that (i) incorporation of Cr ions into the skeleton of SBA-15 is likely for *x*Cr-SBA-15 with Cr surface density $\leq$0.22 Cr-atom/nm^2; (ii) for *y*CrO_x/SBA-15

with Cr surface density ≤0.54 Cr-atom/nm^2, there is high CrO_x dispersion on SBA-15; and (iii) monolayer CrO_x coverage occurs on yCrO$_x$/SBA-15 before a Cr surface density of 0.54 Cr-atom/nm^2.

3.2. Surface areas and pore sizes

Table 1 summarizes the physical properties of xCr-SBA-15 and yCrO$_x$/SBA-15. It is seen that the SBA-15 sample possesses high-surface area (796 m^2/g), large pore diameter (5.6 nm), and moderate pore volume (0.98 cm^3/g). Across the xCr-SBA-15 samples, with the incorporation of Cr ions to the framework of SBA-15, there is a rise in surface area and pore volume whereas there is little change in averaged pore size. As for the yCrO$_x$/SBA-15 samples, despite the little change in average pore size, both surface area and pore volume decrease significantly in comparison to those of SBA-15. The drop in surface area and pore volume could be a result of certain amount of SBA-15 pores being blocked by CrO_x. With a rise in "x" or "y", there is gradual increase in Cr surface density. Apparently, there is a slight decline in sample quality of yCrO$_x$/SBA-15 with increasing Cr content; a similar behavior has also been observed by Wang et al. over the Cr-MCM-41 materials [9]. From the n_{Si}/n_{Cr} data of AAS measurement and the nominal n_{Cr}/n_{Cr+Si} values (Table 1), one can realize that the amount of Cr incorporated in the framework of SBA-15 was limited.

The N_2 adsorption–desorption isotherms of xCr-SBA-15 (Fig. 2A) and yCrO$_x$/SBA-15 (Fig. 2C) are rather similar showing a H_1-type broad hysteresis loop in the p/p_0 range of 0.6–0.8. This feature affirms the type-IV isotherms and the presence of well-ordered pores with 2D-hexagonal structure [13]. Apart from the narrow pore size distribution of xCr-SBA-15 with Cr surface density = 0 and 0.53 Cr-atom/nm^2 (Fig. 2B(a) and (g)), the other samples (especially with Cr surface density = 0.71 Cr-atom/nm^2) exhibit broadened pore size distribution (Fig. 2B), which could be due to a change in pore architecture and/or surface morphology as corroborated by the ESEM and TEM results to be disclosed in Section 3.3. As for the yCrO$_x$/SBA-15 (Fig. 2D) samples, besides the similarity in pore size distribution, there is the detection of a new and relatively weak peak at pore diameter = ca. 3 nm, except for the yCrO$_x$/SBA-15 samples with Cr surface density = 0 and 0.54 Cr-atom/nm^2, which might be associated with the related morphological changes; the results suggest the presence of two kinds of mesopore structures: (i) the banana-like SBA-15 with ordered pores and (ii) the irregularly spherical silica with wormhole-like pores as revealed in ESEM and TEM images of Section 3.3. The absence of the ca. 3 nm pores in the CrO_x/SBA-15 sample with Cr surface density = 0.54 Cr-atom/nm^2 might be due to a variation in CrO_x particle morphology and pore shape as the material evolved from long chain-like to short banana-like or spherical architecture.

3.3. Surface morphologies and pore structures

Electron microscopic techniques are ideal tools for the investigation of surface morphologies and pore structures of solid materials. Fig. 3 shows the ESEM and TEM images as well as SAED patterns of the xCr-SBA-15 and yCrO$_x$/SBA-15 samples. It is observed that the as-received SBA-15 possesses a typical long-chain architecture which is 8–28 μm in length and 200–600 nm in diameter (Fig. 3a); the pore structure is regular and highly ordered with a pore size of ca. 5 nm and a wall thickness of 6–7 nm (Fig. 3b). With a rise in Cr surface density from 0 to 0.09 Cr-atom/nm^2 and further to 0.71 Cr-atom/nm^2, the original chain-like morphology transformed into separate sub-units (i.e. short banana-like rods) with length = 1–4 μm and diameter = 200–600 nm (Fig. 3c and e), the well-defined mesoporous channels were still retained in the sample with Cr surface density = 0.09 Cr-atom/nm^2 (Fig. 3d), in agreement with the results reported by Liu et al. [20]. In the Cr-SBA-15 sample with Cr surface density = 0.71 Cr-atom/nm^2, in addition to the presence of rod-like morphology (inset of Fig. 3f), part of the sub-units changed to irregularly spherical particles with well-developed wormhole-like pore structures (Fig. 3f). Similar to the case of xCr-SBA-15, a morphological evolution of the yCrO$_x$/SBA-15 samples with increasing CrO_x deposition was observed. The lengths of microrods in the yCrO$_x$/SBA-15 samples with Cr surface density = 0.24 and 1.11 Cr-atom/nm^2 (Fig. 3g and i) are in the range of 1–3 μm (a little shorter than those of xCr-SBA-15) and the averaged pore size is ca. 3.5 nm as estimated from the TEM images of ordered pore channels without considering the disordered wormhole-like pores (inset of Fig. 3i). As seen in Fig. 3g, i, and j, the morphologies of the samples changed in comparison to those of the samples with lower Cr surface densities and there is the co-presence of banana-like and irregularly spherical particles, part of their pores became wormhole-like and existed in various sizes. Therefore, it is possible that the mean pore diameters measured by N_2 adsorption–desorption (Table 1) are bigger that those estimated just from the TEM photographs. The transformations of SBA-15 from long chain to rod-like and/or irregularly spherical morphology, and from ordered cylindrical pores to wormhole-like pores are induced by the introduction of Cr ions or CrO_x domains. We propose that such a transformation in particle morphology might be associated with the stronger interaction of chromium with silica at higher Cr contents. The formation mechanism deserves further investigation. From the SAED patterns (insets of Fig. 3d, f, h, and j), one can realize that the xCr-SBA-15 and yCrO$_x$/SBA-15 samples are amorphous, except that the Cr-SBA-15 with Cr surface density = 0.71 Cr-atom/nm^2 and the CrO_x/SBA-15 sample with Cr surface density = 1.11 Cr-atom/nm^2 contain a small amount of crystalline Cr_2O_3 as reflected by the appearance of at least two weak diffraction rings in the corresponding SAED patterns (insets of Fig. 3f and j).

3.4. Surface species and chromia structures

3.4.1. XPS studies

Fig. 4 illustrates the Si 2p, O 1s, and Cr 2p XPS spectra of the xCr-SBA-15 and yCrO$_x$/SBA-15 samples. For the Cr-incorporated samples, symmetric Si 2p and O 1s peaks are respectively observed at binding energy (BE) = ca. 104 eV (Fig. 4A) and ca.

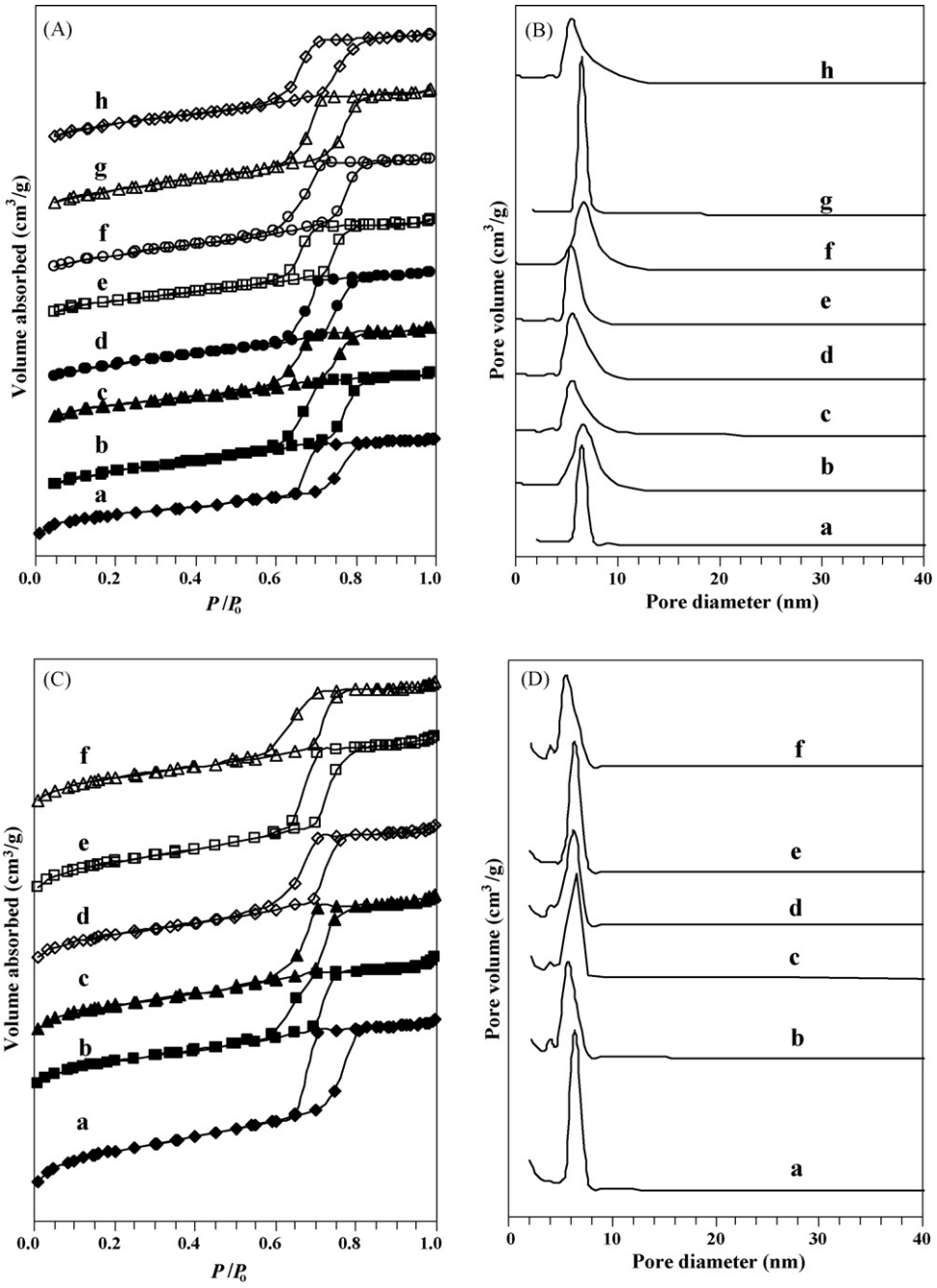

Fig. 2. (A and C) N_2 adsorption–desorption isotherms and (B and D) pore size distributions of (A and B) *x*Cr-SBA-15 with Cr surface density = 0 (a), 0.05 (b), 0.09 (c), 0.12 (d), 0.14 (e), 0.22 (f), 0.53 (g), and 0.71 (h) Cr-atom/nm^2, and (C and D) *y*CrO_x/SBA-15 with Cr surface density = 0 (a), 0.15 (b), 0.24 (c), 0.31 (d), 0.54 (e), and 1.11 (f) Cr-atom/nm^2.

533 eV (Fig. 4B) with only small variation in signal intensity. There are no signals attributable to surface lattice oxygen of CrO_x whose BE should be around 530 eV, affirming that the Cr ions were incorporated into the framework of SBA-15. Over the *y*CrO_x/SBA-15 samples, the BE (ca. 104 eV) of the Si 2p signals remained almost unchanged (Fig. 4D) whereas the O 1s signal shifted from BE = 533.2 eV for CrO_x/SBA-15 with Cr surface density = 0.15 Cr-atom/nm^2 to BE = 532.3 eV for CrO_x/SBA-15 with Cr surface density = 1.11 Cr-atom/nm^2, and there is a decline in O 1s peak symmetry with an increase in Cr content (Fig. 4E). The shift of O 1s peak position towards lower binding energy indicates the possible generation of CrO_x domains and/or Cr_2O_3 crystallites on the *y*CrO_x/SBA-15 sample with Cr surface density = 1.11 Cr-atom/nm^2 where there is the appearance of crystalline Cr_2O_3 phase. These results indicated that there is the aggregation of CrO_x species at elevated Cr contents. The shift in O 1s binding energy of supported CrO_x samples is due to the fact that the local environment of oxygen in SBA-15 and that in CrO_x domain are different. With the rise in Cr content, there is the tendency of generating polychromate species and Cr_2O_3 crystallites. The O 1s binding energy of SBA-15 is ca. 533 eV, whereas that of Cr_2O_3 or dichromate in

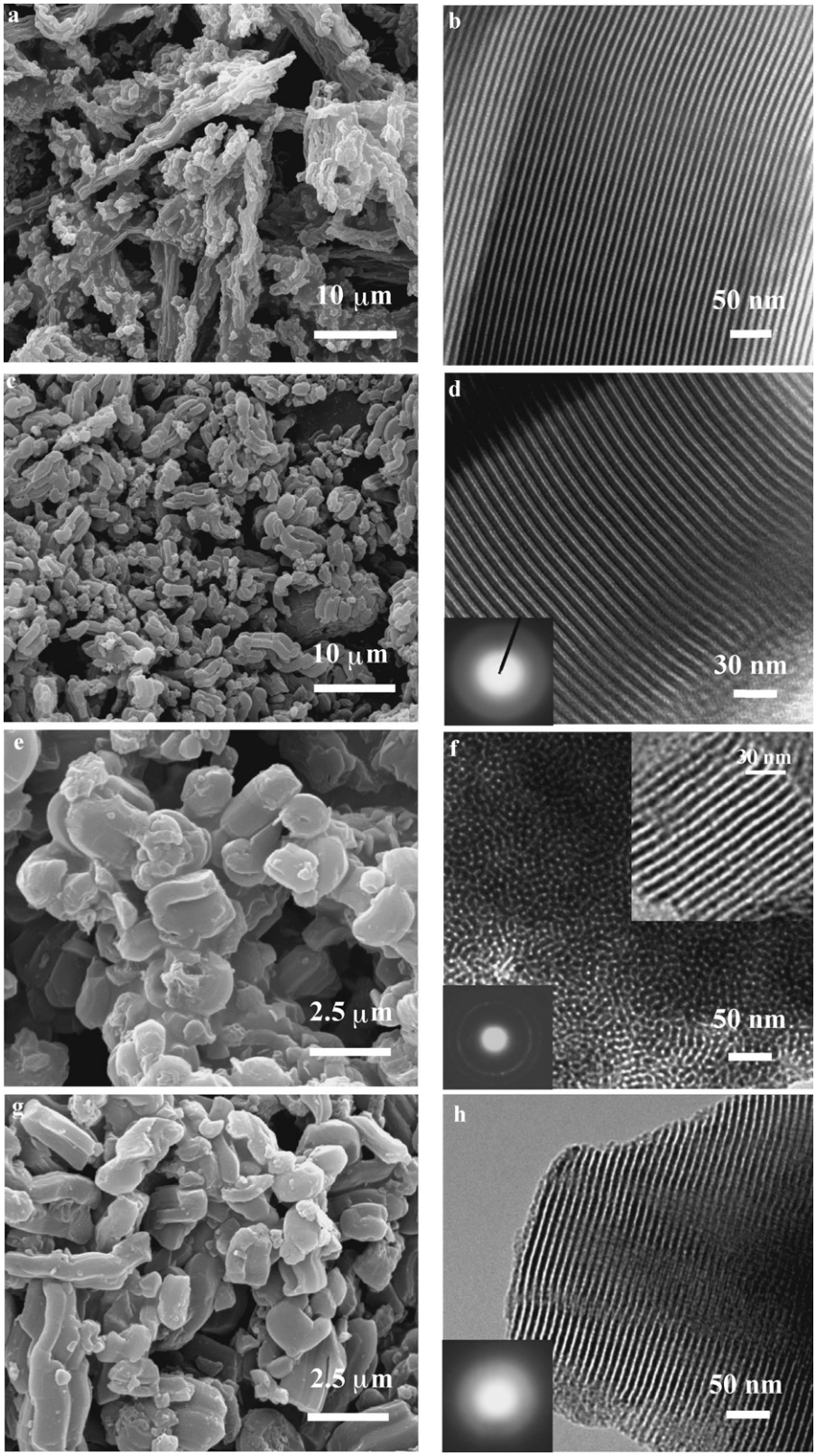

Fig. 3. ESEM (a, c, e, g, i) and TEM (b, d, f, h, j) images of SBA-15 (a and b), *x*Cr-SBA-15 with Cr surface density = 0.09 (c and d) and 0.71 (e and f) Cr-atom/nm^2, and *y*CrO_x/SBA-15 with Cr surface density = 0.15 (g and h) and 1.11 (i and j) Cr-atom/nm^2.

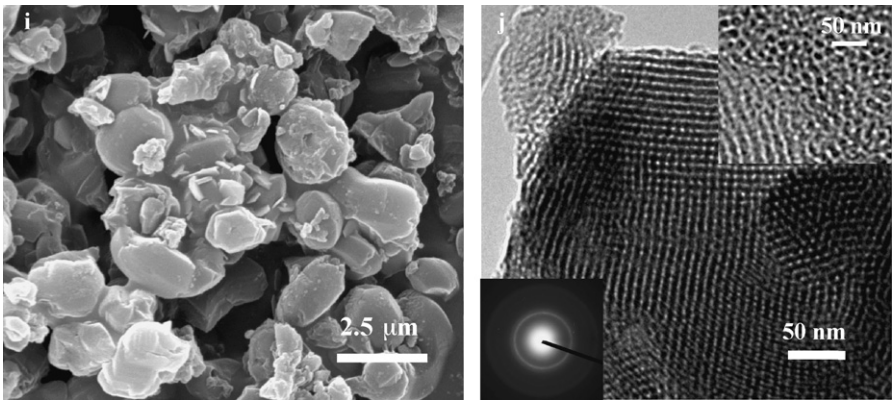

Fig. 3. (*Continued*).

the 529.8–530.5 eV range. Therefore, the O 1s binding energy of yCrO$_x$/SBA-15 shifted from ca. 533 eV to a lower value with increasing Cr concentration. In the case of Cr-SBA-15, however, with most of the Cr ions incorporated into the skeleton of SBA-15, the local co-ordination environment of surface oxygen would be rather similar to that of SBA-15, and thus their O 1s binding energies close to that of SBA-15 (ca. 533 eV). Similar phenomena have been reported by Reddy et al. who detected an O1s BE of 532.8 eV over a Cr-Ti-MCM-41 sample [28].

It has been reported that Cr ions exist in various oxidation states in supported chromia materials, in which Cr^{6+} and Cr^{3+} are believed to participate in redox processes in the catalytic oxidative dehydrogenation of alkanes [37–39]. An investigation on the oxidation states of Cr ions in/on catalysts is beneficial for the elucidation of the nature of the active sites.

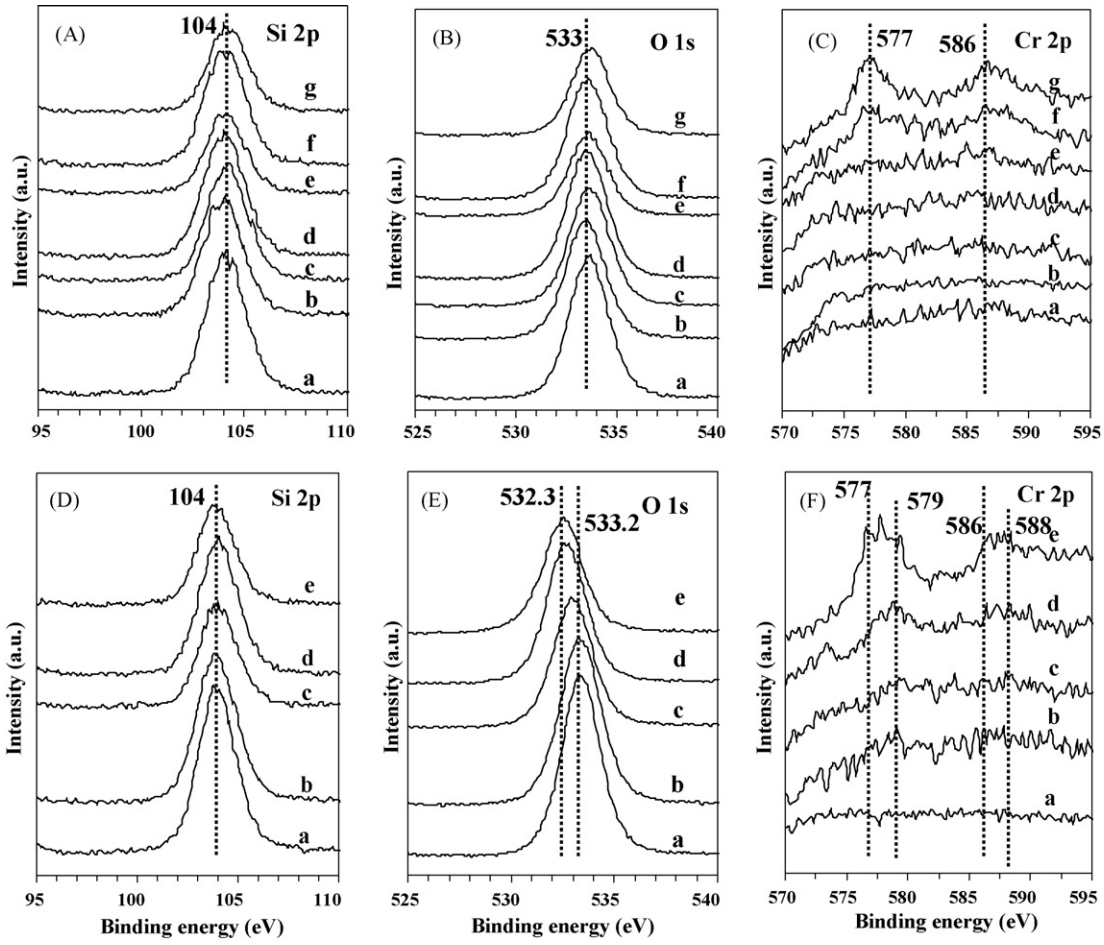

Fig. 4. (A and D) Si 2p, (B and E) O 1s, (C and F) Cr 2p XPS spectra of xCr-SBA-15 (A–C) with Cr surface density = 0.05 (a), 0.09 (b), 0.12 (c), 0.14 (d), 0.22 (e), 0.53 (f), and 0.71 (g) Cr-atom/nm^2, and yCrO$_x$/SBA-15 (D–F) with Cr surface density = 0.15 (a), 0.24 (b), 0.31 (c), 0.54 (d), and 1.11 (e) Cr-atom/nm^2.

According to what have been reported in the literature [38–41], Cr 2p signals at BE = 577 and 586 eV could be assigned to Cr^{3+} ions whereas those at BE = 579 and 588 eV to Cr^{6+} ions. Over *x*Cr-SBA-15 with Cr surface density $\leq$0.22 Cr-atom/nm^2 (Fig. 4C(a–e)), there was no detection of Cr 2p signals, indicating that the Cr species were dispersed in the bulk of SBA-15; at Cr surface density $\geq$0.53 Cr-atom/nm^2, broad signals at BE = 577 and 586 eV appeared, ascribable to Cr^{3+} ions of Cr_2O_3 and there was an obvious increase in Cr 2p intensity due to the enrichment of surface Cr_2O_3 with a rise in Cr surface density from 0.53 to 0.71 Cr-atom/nm^2 (Fig. 4C(e and f)). The result coincides with the results of XRD investigation. Over the *y*CrO_x/SBA-15 samples, the intensities of Cr 2p signals were weak when Cr surface density $\leq$0.31 Cr-atom/nm^2 (Fig. 4F(a–c)); however, with Cr surface density $\geq$0.54 Cr-atom/nm^2 (Fig. 4F(d and e)), Cr 2p signals were detected. The asymmetrical peaks at BE = 575–580 and 585–589 eV could be decomposed into two sets of components with BE = ca. 577 and 579 eV and BE = ca. 586 and 588 eV, respectively. That is to say, there was the co-presence of Cr^{3+} and Cr^{6+} ions [40–43]. The intensity of the Cr^{3+} signals increased whereas that of the Cr^{6+} signals decreased when there was a rise in Cr surface density from 0.54 to 1.11 Cr-atom/nm^2 (Fig. 4F(d and e)). The result is indicative of the formation of crystalline Cr_2O_3 and is in agreement with the results obtained in the XRD.

3.4.2. Laser Raman studies

It is generally accepted that there are three kinds of chromium species, i.e. isolated monochromate, polychromate, and crystal Cr_2O_3 in supported chromium oxides. The Raman bands at 220, 360, 955, and 986 cm^{-1} are attributable to monochromate species in Cr^{6+} state [38,44–47], the ones at 750–1010 cm^{-1} to Cr^{6+} species in the form of polychromate with different degrees of oligomerization [2,44,45,48–52], whereas the ones at 550–640 cm^{-1} to crystal Cr_2O_3 [45,53]. Fig. 5A shows the Raman spectra of hydrated *x*Cr-SBA-15 samples. One can observe that with Cr surface density $\leq$0.22 Cr-atom/nm^2 (Fig. 5A(a–e)), there are Raman bands at 896 (weak), 970 (strong), and 1061 (weak) cm^{-1} attributable to Cr^{6+} species [2,44,45,48–52], and the band at 970 cm^{-1} is smaller in Raman shift than that at 980 cm^{-1} which is due to the Cr–O stretching of monochromate species in Cr-MCM-41 [2,9]. Therefore, we assign tentatively the signal to the Cr–O stretching of monochromate (CrO_4^{2-}) species. Further rise in Cr content (Cr surface density = 0.53–0.71 Cr-atom/nm^2) gave rise to the appearance of two bands at ca. 548 and 641 cm^{-1} that could be ascribed to the crystal phase of Cr_2O_3 (Fig. 5A(g and h)) [53]. Shown in Fig. 5B are the Raman spectra of hydrated and *y*CrO_x/SBA-15 samples. It is observed that there are Raman bands at ca. 880 and 1001 cm^{-1} assignable to monochromate species [45,47] (Fig. 5B(a)). With rise in chromia loading (Fig. 5B(b–e)), there is an overall rise in band intensity, indicating the enhanced presence of the chromia species. Several new Raman bands appeared at ca. 355 (or 362), 550, 610, 840, 893, 955, and 1038 cm^{-1}, in which the band at 355 or 362 cm^{-1} could be ascribed to Cr^{6+} [44], the ones at 550 and 610 cm^{-1} to crystalline Cr_2O_3 [53], the one at 893 cm^{-1} to the Cr–O vibration of hydrated dichromate [2], the ones at 840 and 955 cm^{-1} to the Cr–O vibrations of hydrated trichromate [2,52,54], and the one at 1038 cm^{-1} (due to symmetric stretching of the O=Cr=O group in chromates) to polychromate [47]. At a Cr surface density of 1.11 Cr-atom/nm^2 (Fig. 5B(e)), there are only Raman bands at 550 and 610 cm^{-1}, indicating that with the aggregation of monochromate and polychromate species, the presence of crystalline Cr_2O_3 species became

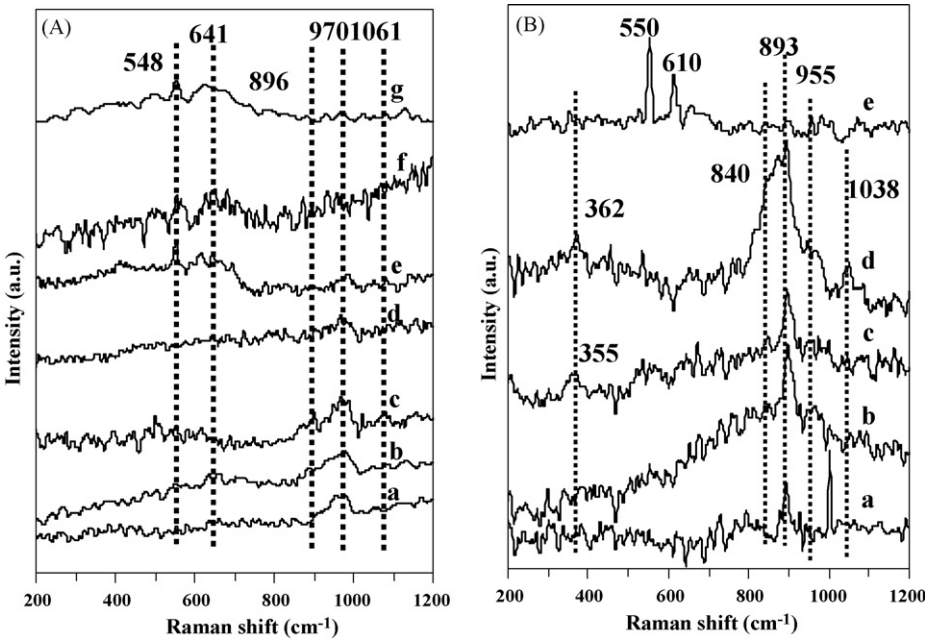

Fig. 5. Raman spectra of (A) *x*Cr-SBA-15 with Cr surface density = 0.05 (a), 0.09 (b), 0.12 (c), 0.14 (d), 0.22 (e), 0.53 (f), and 0.71 (g) Cr-atom/nm^2, and (B) *y*CrO_x/SBA-15 with Cr surface density = 0.15 (a), 0.24 (b), 0.31 (c), 0.54 (d), and 1.11 (e) Cr-atom/nm^2.

dominant. These results are in good agreement with the outcomes of wide-angle XRD analysis. From the Raman results, one can deduce that a monolayer surface coverage of chromia on the SBA-15 support might be achieved at a Cr surface density between 0.54 and 1.11 Cr-atom/nm^2 where a small amount of crystalline chromia could have been formed.

3.4.3. UV–vis studies

Fig. 6 illustrates the UV–vis spectra of the SBA-15, *x*Cr-SBA-15 and *y*CrO_x/SBA-15 samples. For SBA-15, there was only one very weak band at 220 nm (Fig. 7A(a)) which is due to charge transfer characteristics of UV absorption of the SBA-15 skeleton. After Cr incorporation, four absorption bands at ca. 254, 359, 472, and 609 nm (Fig. 6A(b–h)) were detected over *x*Cr-SBA-15, the location of the former three bands suggests the presence of monochromate (Cr^{6+}) species [2,9,11,27,55,56], whereas the last band is a result of d–d transitions of Cr^{3+} species [2,9,11,55]. The band at 609 nm was rather broad (Fig. 6A(b–f)), the intensities of the absorption bands at ca. 254 and 359 nm decreased slightly with an increase in Cr surface density from 0.05 to 0.22 Cr-atom/nm^2, indicating a decline in Cr^{6+} content; the intensity of the band at 609 nm increases with increasing Cr doping (Fig. 6A(b–h)), indicating the rise in Cr^{3+} content. It is also observed that with the formation of crystalline Cr_2O_3, the 254 nm band shifts to a higher wavelength (ca. 280 nm) at Cr surface density = 0.53 and 0.71 Cr-atom/nm^2 (Fig. 6A(g and h)). For the *y*CrO_x/SBA-15 samples with Cr surface density $\leq$0.54 Cr-atom/nm^2 (Fig. 6B(a–d)), there are UV–vis absorption bands at ca. 265, 360, 450–470, and 610–630 nm, the former three bands could be assigned to charge transfer from O^{2-} to Cr^{6+} of tetrahedrally coordinated Cr-oxide moieties [31]. The bands at 265 and 360 nm are attributable to $^1A_1 \rightarrow {}^1T_2$ transition of tetrahedral Cr-oxide, the one at 450–470 nm is due to the symmetry-forbidden nature of the $^1A_1 \rightarrow {}^1T_1$ transition of tetrahedral Cr-oxide [32], and the one at 610–630 nm to the $A_{2g} \rightarrow T_{2g}$ transition typical of octahedrally coordinated Cr^{3+} in Cr_2O_3 clusters [33]. It is apparent that the amount of octahedrally coordinated Cr^{3+} is rather low in samples with Cr surface density $\leq$0.54 Cr-atom/nm^2. When the Cr surface density increases to 1.11 Cr-atom/nm^2, the corresponding UV–vis absorption profile (Fig. 6B(e)) is basically that of crystal Cr_2O_3 (Fig. 6B(f)). The results indicated that Cr^{6+} species of mono- and poly-chromate existed in *y*CrO_x/SBA-15 with Cr surface density $\leq$0.54 Cr-atom/nm^2, whereas there was the presence of octahedral Cr^{3+} (of Cr_2O_3) when Cr surface density was higher than 0.54 Cr-atom/nm^2. These results agree well with those obtained in the XPS and Raman studies.

3.4.4. FT-IR studies

FT-IR spectroscopy is a useful technique for characterizing Cr species incorporated in the framework of porous materials. There were strong and broad bands centered at 3410 cm^{-1} (not shown here) assignable to surface silanols and adsorbed water [57]. Fig. 7 shows the FTIR results of the *x*Cr-SBA-15 and *y*CrO_x/SBA-15 samples. The bands at 1618–1620 cm^{-1} could also be ascribed to adsorbed water; the bands at 453–457, 550–604, 784–794, 1072–1076, and 1383–1384 cm^{-1} arose from Si–O–Si vibration of SBA-15 framework [58]. The IR band at ca. 966 cm^{-1} has been assigned before to Si–O vibration in a Si–OH group of pure siliceous MCM-41 [59] and the one at ca. 956 cm^{-1} to O–Cr(VI) in Cr-SBA-1 [60]. In the present study, there is a shift of the IR band to ca. 941 and 950 cm^{-1} (much lower than 960 cm^{-1}) in the Cr-SBA-15 and CrO_x/SBA-15 samples, respectively. It might be due to the difference in local environment of Cr-SBA-15, CrO_x/SBA-15, Cr-SBA-1, and

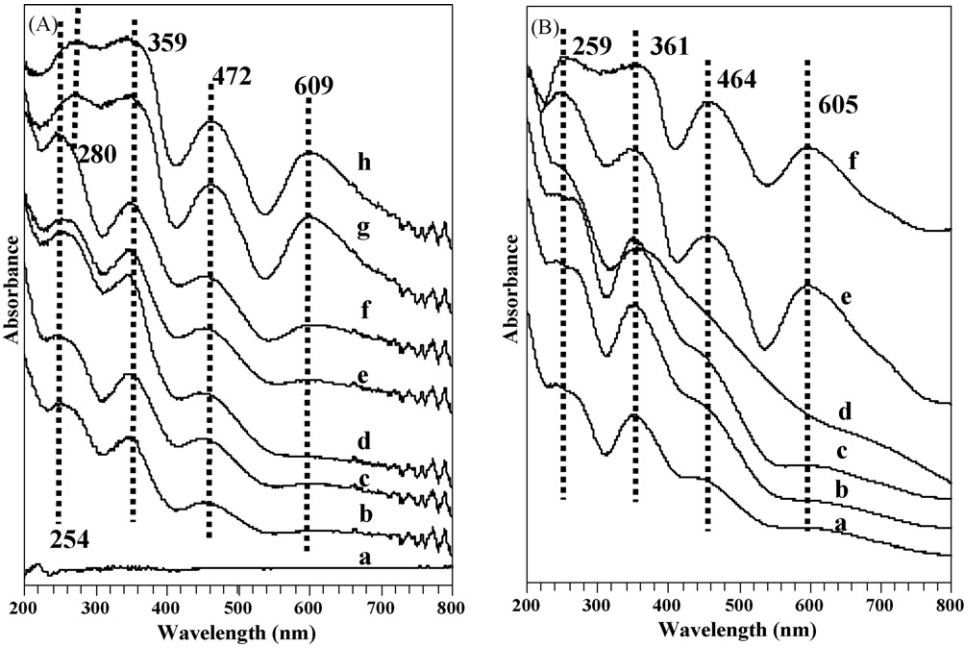

Fig. 6. UV–vis spectra of (A) *x*Cr-SBA-15 with Cr surface density = 0 (a), 0.05 (b), 0.09 (c), 0.12 (d), 0.14 (e), 0.22 (f), 0.53 (g), and 0.71 (h) Cr-atom/nm^2, and (B) *y*CrO_x/SBA-15 with Cr surface density = 0.15 (a), 0.24 (b), 0.31 (c), 0.54 (d), and 1.11 (e) Cr-atom/nm^2, and crystal Cr_2O_3 (f).

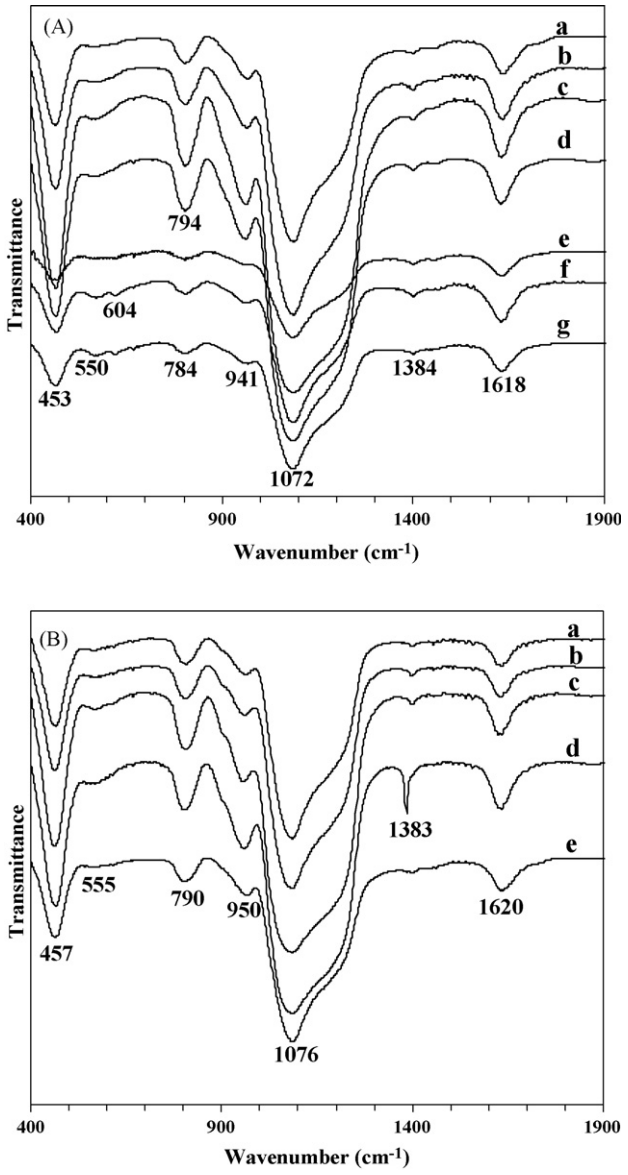

Fig. 7. FT-IR spectra of (A) *x*Cr-SBA-15 with Cr surface density = 0.05 (a), 0.09 (b), 0.12 (c), 0.14 (d), 0.22 (e), 0.53 (f), and 0.71 (g) Cr-atom/nm^2, and (B) *y*CrO_x/SBA-15 with Cr surface density = 0.15 (a), 0.24 (b), 0.31 (c), 0.54 (d), and 1.11 (e) Cr-atom/nm^2.

Cr-MCM-41. We assign tentatively this weak absorption signal to O–Cr(VI) vibration. For the *x*Cr-SBA-15 samples, the intensity of the band at 941–950 cm^{-1} increased only slightly from Cr surface density = 0.05 to 0.14 Cr-atom/nm^2 (Fig. 7A(a–d)) but decreased when Cr surface density $\geq$0.22 Cr-atom/nm^2 (Fig. 7A(e–g)), indicating the amounts of Cr^{6+} in the samples with Cr surface densities = 0.05–0.14 Cr-atom/nm^2 are higher than those in the samples with Cr surface densities $\geq$0.22 Cr-atom/nm^2. In the meanwhile, one can also observe that there was a similar trend in the intensity of the adsorption bands at 453, 794, and 1618 cm^{-1}, possibly as a consequence of changes in surface morphology and pore structure with a rise in chromium doping as illustrated in ESEM and TEM investigations (Section 3.3). Similar trends were observed across the *y*CrO_x/SBA-15 samples (in intensities of the 950 cm^{-1} band and those of the other bands), with the "turning phenomenon" occurred when Cr surface density >0.31 Cr-atom/nm^2 (Fig. 7B). The results are agreeable with those obtained in the XPS, Raman, and UV–vis studies.

3.5. Reducibility

The reducibility of a catalyst plays an important role in reactions involving a redox mechanism. Shown in Fig. 8 are the H_2-TPR profiles of the *x*Cr-SBA-15 and *y*CrO_x/SBA-15 samples. Under equal experimental condition, no reduction band was observed over the SBA-15 support and only one reduction band centered at 670 °C was recorded over the pure alpha Cr_2O_3 (not shown here). Over *x*Cr-SBA-15, only one single reduction band centered at ca. 520, 512, 500, 520, 525, 540, and 537 °C was observed for Cr surface density = 0.05, 0.09, 0.12, 0.14, 0.22, 0.53, and 0.71 Cr-atom/nm^2, respectively (Fig. 8A(a–g)), corresponding to a total H_2 consumption of 0.11, 0.30, 0.49, 0.74, 1.08, 1.28, and 1.01 mmol/g_{cat}. These reduction signals are due to the reduction of Cr^{6+} to Cr^{3+} ions [11,55,56], and according to the $Cr^{6+} \rightarrow Cr^{3+}$ reaction the estimated H/Cr atomic ratio was 2.96, 2.95, 2.91, 2.92, 2.90, 2.85, and 2.34, respectively. The reduction temperature first decreased and then increased, with the lowest temperature at 500 °C over the Cr-SBA-15 sample with Cr surface density = 0.12 Cr-atom/nm^2; the amount of reducible Cr species increased until the Cr surface density reached 0.53 Cr-atom/nm^2 and then decreased due to the formation of crystal Cr_2O_3 phase. In the case of *y*CrO_x/SBA-15, there was only one reduction band centered at ca. 486, 480, 470, 464, and 495 °C for Cr surface density = 0.15, 0.24, 0.31, 0.54, and 1.11 Cr-atom/nm^2, respectively (Fig. 8B(a–e)), the corresponding H_2 consumption was 0.19, 0.31, 0.92, 2.39, and 1.90 mmol/g_{cat}, and based on the reduction of Cr^{6+} to Cr^{3+} the H/Cr atomic ratio was estimated to be 2.97, 2.88, 2.81, 2.62, and 2.21, respectively. One can detect that the CrO_x/SBA-15 sample with Cr surface density = 0.54 Cr-atom/nm^2 is the lowest in reduction temperature and the largest in reducible chromia amount. The theoretical value of H/Cr atomic ratio is three if one considers that the reduction process undergoes via $Cr^{6+} \rightarrow Cr^{3+}$. It is understandable that there are (i) mainly Cr^{6+} species in the *x*Cr-SBA-15 samples with Cr surface density $\leq$0.22 Cr-atom/nm^2 and in the *y*CrO_x/SBA-15 samples with Cr surface density <0.15 Cr-atom/nm^2; and (ii) co-existence of Cr^{6+} and Cr^{3+} species when Cr surface density is higher than the above values. It has been reported that for chromium oxides deposited on or incorporated into zeolite or oxide materials, a higher temperature is needed to reduce the highly dispersed Cr species [55,61]. The higher reduction temperature of *x*Cr-SBA-15 in comparison to those of *y*CrO_x/SBA-15 suggests that there is better dispersion of Cr species in the former case. Compared to alpha Cr_2O_3 crystal, the mono- and poly-chromate species are more reducible and the latter exhibits higher reducibility than the former in the case of Cr-MCM-41 materials [62]. It is rather similar in the case of Cr-SBA-15. Despite some authors reported a lower reduction temperature over bulk alpha Cr_2O_3 [4,63], we observed the reduction of pure α-Cr_2O_3 at 670 °C in

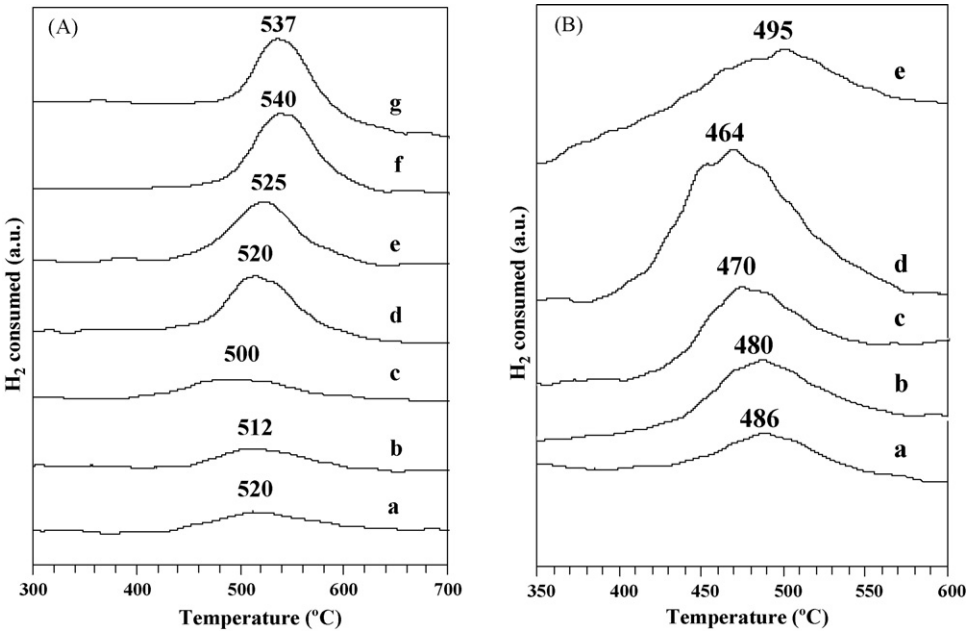

Fig. 8. H_2-TPR profiles of (A) *x*Cr-SBA-15 with Cr surface density = 0.05 (a), 0.09 (b), 0.12 (c), 0.14 (d), 0.22 (e), 0.53 (f), and 0.71 (g) Cr-atom/nm^2, and (B) *y*CrO_x/SBA-15 with Cr surface density = 0.15 (a), 0.24 (b), 0.31 (c), 0.54 (d), and 1.11 (e) Cr-atom/nm^2.

our H_2-TPR measurement system. As for the higher reduction temperatures of our Cr-containing samples, there are several authors who observed the reduction of Cr-MCM-41 (by H_2) in the 440–540 °C range [62] and the reduction of Cr-MSU-1 and Cr/MSU-1 (by H_2) in the 350–600 °C range [30]. As shown in XPS and Raman studies, the main surface CrO_x species are monochromate and polychromate with Cr surface density $\leq$0.54 Cr-atom/nm^2, whereas they are polychromate and crystalline Cr_2O_3 when Cr surface density $\geq$1.11 Cr-atom/nm^2. The H/Cr atomic ratios of less than three calculated from the TPR data further confirm the co-presence of Cr^{6+} and Cr^{3+} ions [4,40,53] in the *y*CrO_x/SBA-15 samples with surface density $\geq$0.24 Cr-atom/nm^2, in agreement with the results obtained in the laser Raman and XPS investigations.

4. Conclusions

Based on the above results and discussion, it is concluded:

(1) Cr-incorporated SBA-15 and CrO_x/SBA-15 can be generated with well-ordered mesoporous structures and highly dispersed Cr or CrO_x species.
(2) The surface morphologies of *x*Cr-SBA-15 and *y*CrO_x/SBA-15 changed from long chain-like to short banana-like and further to an irregularly spherical architecture with increasing Cr surface density.
(3) The Cr species in *x*Cr-SBA-15 and *y*CrO_x/SBA-15 existed mainly in 6+ oxidation state (i.e. mono- and poly-chromate) at Cr surface density $\leq$0.22 Cr-atom/nm^2 for the former and Cr surface density $\leq$0.54 Cr-atom/nm^2 for the latter, but further increase in Cr surface density would result in the Cr^{3+} species (i.e. Cr_2O_3) becoming dominant.
(4) Maximal Cr incorporation can be achieved at Cr surface density $\leq$0.53 Cr-atom/nm^2 whereas one monolayer surface CrO_x coverage occurs at Cr surface density $<$1.11 Cr-atom/nm^2.
(5) The reducibility of *y*CrO_x/SBA-15 is higher than that of *x*Cr-SBA-15, with the highest reducibility observed at Cr surface density of 0.54 and 0.12 Cr-atom/nm^2, respectively, over the two series of materials investigated.

Acknowledgement

The work described above was supported by the National Natural Science Foundation of China (Grant No. 20473006) and Funding Project for Academic Human Resources Development in Institutions of Higher Learning under the Jurisdiction of Beijing Municipality (PHR (IHLB)).

References

[1] J. Muzart, Chem. Rev. 92 (1992) 113.
[2] B.M. Weckhuysen, I.E. Wachs, R.A. Schoonheydt, Chem. Rev. 96 (1996) 3327.
[3] L.R. Mentasty, O.F. Gorriz, L.E. Cadus, Ind. Eng. Chem. Res. 38 (1999) 396.
[4] A. Hakuli, M.E. Harlin, L.B. Backman, A.O.I. Krause, J. Catal. 184 (1999) 349.
[5] H. Yamashita, K. Yoshizawa, M. Ariyuki, S. Higashimoto, M. Che, M. Anpo, Chem. Commun. (2001) 435.
[6] A.A. Ismail, I.A. Ibrahim, R.M. Mohamed, Appl. Catal. B 45 (2003) 161.
[7] C.T. Kresge, M.E. Leonowicz, W.J. Roth, J.C. Vartuli, J.S. Beck, Nature 359 (1992) 710.
[8] J.S. Beck, J.C. Vartuli, W.J. Roth, M.E. Leonowicz, C.T. Kresge, K.D. Schmitt, C.T-W. Chu, D.H. Olson, E.W. Sheppard, S.B. McCullen, J.B. Higgins, J.L. Schlenker, J. Am. Chem. Soc. 114 (1992) 10834.
[9] Y. Wang, Y. Ohishi, T. Shishido, Q.H. Zhang, W. Yang, Q. Guo, H.L. Wan, K. Takehira, J. Catal. 220 (2003) 347.
[10] M.L. Peña, A. Dejoz, V. Fornés, F. Rey, M.I. Vázquez, J.M. López Nieto, Appl. Catal. A 209 (2001) 155.

[11] K. Takehira, Y. Ohishi, T. Shishido, T. Kawabata, K. Takaki, Q. Zhang, Y. Wang, J. Catal. 224 (2004) 404.
[12] D. Zhao, J. Feng, Q. Huo, N. Melosh, G.H. Fredrickson, B.F. Chmelka, G.D. Stuky, Science 279 (1998) 548.
[13] D. Zhao, Q. Huo, J. Feng, B.F. Chmelka, G.D. Stuky, J. Am. Chem. Soc. 120 (1998) 6024.
[14] A. Vinu, D.P. Sawant, K. Ariga, K.Z. Hossain, S.B. Halligudi, M. Hartmann, M. Nomura, Chem. Mater. 17 (2005) 5339.
[15] P. Wu, T. Tatsumi, Chem. Mater. 14 (2002) 1657.
[16] G. Li, X.S. Zhao, Ind. Eng. Chem. Res. 45 (2006) 3569.
[17] A. Vinu, P. Srinivasu, M. Miyahara, K. Ariga, J. Phys. Chem. B 110 (2006) 801.
[18] Y. Yue, A. Gédéon, J.-L. Bonardet, N. Melosh, J.-B. D'Espinose, J. Fraissard, Chem. Commun. (1999) 1967.
[19] Y. Li, W. Zhang, L. Zhang, Q. Yang, Z. Wei, Z. Feng, C. Li, J. Phys. Chem. B 108 (2004) 9739.
[20] Y.-M. Liu, Y. Cao, N. Yi, W.-L. Feng, W.-L. Dai, S.-R. Yan, H.-Y. He, K.-N. Fan, J. Catal. 224 (2004) 417.
[21] C. Hess, J.D. Hoefelmeyer, T.D. Tilley, J. Phys. Chem. B 108 (2004) 9703.
[22] Y. Sun, S. Walspurger, J.-P. Tessonnier, B. Louis, J. Sommer, Appl. Catal. A 300 (2006) 1.
[23] Y. Segura, P. Cool, P. Van Der Voort, F. Mees, V. Meynen, E.F. Vansant, J. Phys. Chem. B 108 (2004) 3794.
[24] Y. Segura, L. Chmielarz, P. Kustrowski, P. Cool, R. Dziembaj, E.F. Vansant, Appl. Catal. B 61 (2005) 69.
[25] W.-H. Zhang, J. Lu, B. Han, M. Li, J. Xiu, P. Ying, C. Li, Chem. Mater. 14 (2002) 3413.
[26] B.L. Newalkar, J. Olanrewaju, S. Komarneni, Chem. Mater. 13 (2001) 552.
[27] Z. Zhu, Z. Chang, L. Kevan, J. Phys. Chem. B 103 (1999) 2680.
[28] E.P. Reddy, L. Davydov, P.G. Smirniotis, J. Phys. Chem. B 106 (2002) 3394.
[29] P. Kuśtrowski, L. Chmielarz, R. Dziembaj, P. Cool, E.F. Vansant, J. Phys. Chem. B 109 (2005) 11552.
[30] L. Liu, H. Li, Y. Zhang, Catal. Today 115 (2006) 235.
[31] B.M. Weckhuysen, A.A. Verberckmoes, A.L. Buttiens, R.A. Schoonheydt, J. Phys. Chem. 98 (1994) 579.
[32] A. Lannibello, S. Marengo, P. Tittarelli, G. Morelli, A. Zecchina, J. Chem. Soc. Faraday Trans. I 80 (1984) 2209.
[33] L. Chmielarz, P. Kustrowski, M. Kruszec, R. Dziembaj, P. Cool, E.F. Vansant, J. Porous Mater. 12 (2005) 183.
[34] S.B. Deng, R.B. Bai, Water Res. 38 (2004) 2424.
[35] M.M. Hoffmann, J.G. Darab, J.L. Fulton, J. Phys. Chem. A 105 (2001) 6876.
[36] M. Selvaraj, S. Kawi, Chem. Mater. 19 (2007) 509.
[37] S. Derossi, G. Ferraris, S. Fremiotti, E. Garrone, G. Ghiotti, M.C. Campa, V. Indovina, J. Catal. 148 (1994) 36.
[38] D.S. Kim, I.E. Wachs, J. Catal. 142 (1993) 166.
[39] A. Hakuli, A. Kytökivi, A.O.I. Krause, Appl. Catal. A 190 (2000) 219.
[40] B. Liu, M. Terano, J. Mol. Catal. A 172 (2001) 227.
[41] A. Hakuli, A. Kytokivi, A.O.I. Krause, T. Suntola, J. Catal. 161 (1996) 393.
[42] X. Zhao, X. Wang, Catal. Commun. 7 (2006) 633.
[43] F. Cavani, M. Koutyrev, F. Trifirò, A. Bartolini, D. Ghisletti, R. Iezzi, A. Santucci, G. Del Piero, J. Catal. 158 (1996) 236.
[44] M.A. Vuurman, D.J. Stufkens, A. Oskam, J.A. Moulijn, F. Kapteijn, J. Mol. Catal. 60 (1990) 83.
[45] M.A. Vuurman, I.E. Wachs, J. Phys. Chem. 96 (1992) 5008.
[46] D.S. Kim, J.-M. Tatibouet, I.E. Wachs, J. Catal. 136 (1992) 209.
[47] S. Yang, E. Iglesia, A.T. Bell, J. Phys. Chem. B 109 (2005) 8987.
[48] H.H. Kung, Adv. Catal. 40 (1994) 1.
[49] G. Deo, I.E. Wachs, J. Phys. Chem. 95 (1991) 5889.
[50] F.D. Hardcastle, I.E. Wachs, J. Mol. Catal. 46 (1988) 173.
[51] M.A. Vuurman, I.E. Wachs, D.J. Stufkens, A. Oskam, J. Mol. Catal. 80 (1993) 209.
[52] M.A. Vuurman, F.D. Hardcastle, I.E. Wachs, J. Mol. Catal. 84 (1993) 193.
[53] M. Cherian, M.S. Rao, A.M. Hirt, I.E. Wachs, G. Deo, J. Catal. 211 (2002) 482.
[54] B. Grzybowska, J. Słoczyński, R. Grabowski, K. Wcisło, A. Kozłowska, J. Stoch, J. Zieliński, J. Catal. 178 (1998) 687.
[55] A.B. Gaspar, J.L.F. Brito, L.C. Dieguez, J. Mol. Catal. A 203 (2003) 251.
[56] A. Jiménez-López, E. Rodrigues-Castellón, P. Maireles-Torres, L. Diaz, J. Mérida-Robles, Appl. Catal. A 218 (2001) 295.
[57] S. Samanta, N.K. Mal, A. Bhaumik, J. Mol. Catal. A 236 (2005) 7.
[58] H.Y. Le, W.M. Hua, Y. Tang, Y.H. Le, Z. Gao, Chem. J. Chin. Univ. 21 (2000) 1101.
[59] S. Schwarz, D.R. Corbin, A.J. Vega, in: R.F. Lobo, J.S. Beck, S.L. Suib, D.R. Corbin, M.E. Davis, L.E. Iton, S.I. Zones (Eds.), Proc. Mater. Res. Soc. Symp., vol. 431, Mater. Res. Soc., Pittsburgh, PA, 1996, p. 137.
[60] X. Zhao, X. Wang, J. Mol. Catal. A 261 (2007) 225.
[61] C.M. Pradier, F. Rodrigues, P. Marcus, M.V. Landau, M.L. Kaliya, A. Gutman, M. Herskowitz, Appl. Catal. B 27 (2000) 73.
[62] M. Lezanska, G.S. Szymanski, P. Pietrzyk, Z. Sojka, J.A. Lercher, J. Phys. Chem. C 111 (2007) 1830.
[63] M. Cherian, M.S. Rao, W.-T. Yang, J.-M. Jehng, A.M. Hirt, G. Deo, Appl. Catal. A 233 (2002) 21.